The challenging case of the turbulent flow around a thin plate wind deflector, and its numerical prediction by LES and RANS models

Luiz Eduardo B. Sampaio [a], André Luiz T. Rezende [b], Angela O. Nieckele [c,*]

[a] Laboratory of Theoretical and Applied Mechanics – LMTA/PGMEC, Universidade Federal Fluminense – UFF, Rua Passo da Pátria 156 (bl E, s 216), Niterói, RJ 24210-240, Brazil
[b] Department of Mechanical Engineering, Instituto Militar de Engenharia – IME, Praça General Tibúrcio 80, Urca, Rio de Janeiro, RJ 22290-270, Brazil
[c] Department of Mechanical Engineering, Catholic University of Rio de Janeiro, PUC-Rio, Rua Marquês de São Vicente 225, Gávea, Rio de Janeiro, RJ 22451-900, Brazil

ARTICLE INFO

ABSTRACT

The long recirculation bubble found in many industrial applications, mostly involving thin airfoils and thin plate wind deflectors, presents a challenging case for numerical models based on RANS methodology. A deeper understanding of this methodology and its limitations is gained through a series of numerical simulations of the incompressible flow around a thin flat plate of infinite wingspan at small incidences. In this numerically challenging flow, a thin recirculation zone with highly anisotropic turbulent structures is formed close to the leading edge after boundary layer separation. The importance of capturing anisotropy is thoroughly examined and quantitatively assessed in this paper, through a number of simulations employing both large eddy simulations (LES) and Reynolds average Navier–Stokes (RANS) approaches. The former is validated against previous wind tunnel experiment. Since the experimental data does not provide all tensor components to fully assess RANS quality, and LES results can be considered as a reliable source, they are employed in the full characterization of turbulence and in the assessment of the several RANS models predictions presented in this paper. Quantitative results are shown for the errors in capturing the anisotropy part of the Reynolds stress tensor for several RANS models, including Spalart–Almaras, $\kappa - \omega$ SST and transition $k - \omega$ SST.

© 2014 Elsevier Ltd. All rights reserved.

1. Introduction

Long and thin recirculation bubbles are found in many wind engineering and aerodynamic industrial application, such as in thin and membrane airfoils, wind deflectors, yacht sails, small wind turbine generators, orientation fins, microair vehicles, missile and rocket fins, to cite a few (Cyr and Newman, 1996; Lian and Shyy, 2005; Lasher et al., 2005; Lasher and Sonnenmeier, 2008). However, its numerical prediction would still benefit from a more robust, efficient and precise methodology to cope with the physically complex flow, in which one can find features like highly anisotropic turbulent structures, shear layer development and transition to turbulence, separation, reattachment, relaminarization in the backflow, secondary recirculation zones, post-reattachment boundary layer development, etc.

All these features are also present in the flow around the geometrically simpler thin flat plate with a sharp leading edge at shallow incidence, as illustrated in Fig. 1. This simpler test case can thus serve as a benchmark for a critical evaluation of computational turbulence models, ultimately leading to better methodologies and helping the design of industrial devices in all of the afore-mentioned application fields.

The thin airfoil bubble created on a plate with a sharp leading edge is characterized by a flow separation at the leading edge with a reattachment to the upper surface at a point which moves gradually downstream with increasing incidence. If the incidence angle is sufficiently small (usually smaller than 7°), the flow reattaches. As shown in Fig. 1, there is a dividing streamline which separates the bubble from the outer flow and which rejoins the surface at the reattachment point. For greater angles, there is no reattachment point and the bubble enlarges downstream into the wake (Newman and Tse, 1992).

Subsequent to separation, the shear layer distance to the wall increases rapidly, and the action of the viscous damping due to the high gradients in this region becomes weaker. Because of this deficit in the viscous damping, the shear layer is expected to suffer transition very close to the leading edge. The turbulent shear layer thickness increases quickly and has a high entrainment rate; it then reattaches further downstream and bifurcates. Some flow is

* Corresponding author.
E-mail addresses: luizebs@gmail.com (L.E.B. Sampaio), arezende@ime.eb.br (A. Luiz T. Rezende), nieckele@puc-rio.br (A. O. Nieckele).
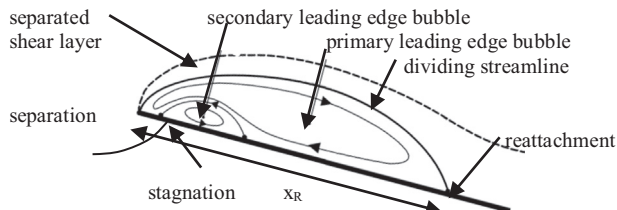
Fig. 1. Simplified model of a thin airfoil separation bubble.

going upstream to feed the shear layer resulting in a pressure reduction at the surface, which in turn helps bend the shear layer towards the reattachment point. The remaining flow is driven directly downstream where it reverts gradually to an attached turbulent boundary layer before reaching the trailing edge.

This complex flow has been investigated experimentally by Crompton (2001) and numerically by Collie et al. (2008). Crompton (2001) measured detailed velocity and turbulence statistics in the leading edge bubble in a wind tunnel with Laser Doppler Anemometry (LDV) for incidence angles ranging from $1°$ to $5°$ and a chord-based Reynolds number (**Re**) of 2.13×10^5. Collie et al. (2008) investigated the performance of the standard $k-\omega$ and $k-\omega$ SST models, by comparing the numerical prediction with Crompton's experimental data.

Crompton (2001) observed that the velocity and pressure fields do not depend too much on the Reynolds number, as long as **Re** $> 1.0 \times 10^5$. The reason for this is that most of the **Re** number dependence is tied to the location of the laminar–turbulent transition point in the shear layer, which will dictate the curvature of this shear layer, and, consequently, the reattachment point, pressure distribution over the plate, and velocity profiles. As the Reynolds number is increased, this transition happens closer and closer to the leading edge, up to a point where it happens almost immediately after separation of the boundary layer, in which case the transition point is virtually at the leading edge. From this point on, it makes no difference how high the Reynolds number is, since the turbulence content will be immediately established, and further filling up of the turbulent spectrum (which would come with an increase in **Re**) would not be relevant, as it is well known that the bigger structures carry most of the energy.

Therefore, when the **Re** is big enough, the turbulence far upstream of the plate is less and less important, as the fast turbulence generation close to the leading edge is responsible for the appearance of almost all the observed velocity fluctuations. For this reason, the experiment of Crompton is an excellent candidate for a benchmark test for numerical simulations of external turbulent aerodynamics, as it does not require a careful representation of the inlet turbulence found in the original wind tunnel. In other circumstances, like in the case of a smoothly curved airfoil operating at lower **Re**, for instance, the wind tunnel turbulence characteristics should be well known, not only in terms of amplitude distribution, but also in terms of its spectrum. In the smooth airfoil case, a small variation in the inlet turbulence might be enough to delay or even prevent a separation of the boundary layer, making it imperative to reproduce as closely as possible the inlet turbulence characteristics in the numerical simulations, if one really wants to make any serious conclusion about the merits of different models.

From an academic point of view, this thin flat plate flow configuration provides an interesting and challenging test case where several aspects of turbulence modeling and numerical schemes can be examined. Because of its rich variety of important turbulent phenomena, especially its strongly anisotropic structures, several traditional turbulence models fail to predict even the simpler first order velocity statistics, pressure coefficients, and critical characteristics such as the

reattachment length. In some ways, it can be considered the external version of the classic backward facing step benchmark test case (Choi and Moin, 1994). In fact, both test cases present a very well-defined point of separation, determined by a sharp edge in the geometry from where a stream of vortices are shed; a principal recirculating structure; and not rarely, further separations and reattachments are observed in the mean velocity field, in the form of secondary recirculation bubbles. However, the level of turbulence anisotropy that can be obtained in the flow around thin flat plate is not achievable by a simple backward facing step configuration. Added to the larger computational domain, which requires several compromises in the mesh design, this external version of the backward facing step can be considered a much more challenging and an important tool for validation and development of better turbulence models for wind engineering and external aerodynamic applications.

Another merit of the case investigated by Crompton is its very simple geometry, easily reproducible, but which presents several of the complex flow structures observed in regular airfoils. For all the above reasons, this experiment of Crompton was chosen in this work as a benchmark for testing the performance of turbulence numerical simulations based on the Reynolds averaging Navier–Stokes methodology (RANS), while investigating the weaknesses of the different models.

The correct simulation of the separation bubble can be accomplished with DNS computations. However, due to their extremely high costs, those are not accessible for this type of flow, and RANS methods become an attractive solution to calculate complex flows (Laurent et al., 2012). However, these methods are based on assumptions that violate some basic physical principles leading to unphysical behaviors. Therefore, a careful analysis of RANS methodology must be performed to understand its applicability and limitations (Han et al., 2012).

The goal of this work is to isolate and understand the implications of the limitations presented by RANS methodology. Several RANS models were tested and compared to experimental data (Crompton, 2001). However, the latter was not complete enough to quantify the RANS discrepancies and identify its sources, as some fluctuation components were not provided. Therefore, Large-Eddy Simulations were performed in order to provide the complementary information needed for this study. LES results correlated very well to the available experimental data, and therefore were considered a reliable source for the assessment of RANS methodology. More specifically, they allowed a quantitative evaluation of how much the RANS anisotropy predictions for the Reynolds stress tensor deviates from the reliable data from LES, and where in the domain these deviations originated. The reason for the special attention to this anisotropy tensor is that it plays a fundamental role in the way the turbulence alters the transport of the averaged linear momentum. Any improvement in this respect will help future improvements to the RANS methodology. Among the several RANS models tested are: Spalart–Allmaras model; $k-\omega$ SST model and two variations of the transition $k-\omega$ SST (one from Fluent (2013), and one from CFX (2013), with intermittence transitional turbulence capturing). The Spalart–Allmaras model was selected since it was designed for external flows and it only solves one additional equation, meaning it should be faster and cheaper. The $k-\omega$ SST was also employed by Collie et al. (2008), and was selected to allow a direct comparison, by employing a finer mesh in order to assess the mesh quality. The decision to employ transition models was based on the expectation of better capturing the secondary bubble. It should be mentioned here that the Reynolds stress model was also tested, in a hope to improve the prediction of the secondary statistics and the flow anisotropic. However, some spurious results also reported in previously literature were observed here, and this investigation was not pursued any further.

This work is organized as follows: Section 2 presents the mathematical formulation for each RANS model tested, as well as

for the LES; Section 3 presents the test case with the plate geometry, and the domain employed in the numerical simulations, with its corresponding boundary conditions; Section 4 describes the numerical details including the discretization schemes employed and the mesh validation performed; Section 5 presents the results obtained; and Section 6 outlines the main conclusions and suggestions for future improvements.

2. Mathematical formulation

The transport equations that describe conservation of momentum and mass for incompressible flows are respectively the Navier–Stokes and continuity equations, which read

$$\frac{\partial \mathbf{u}}{\partial t} + \nabla \cdot (\mathbf{u}\,\mathbf{u}) = -\nabla\left(\frac{p}{\rho}\right) + v\,\nabla^2\,\mathbf{u}; \quad \nabla \cdot \mathbf{u} = 0 \tag{1}$$

with $\mathbf{u}$ being the velocity, p the pressure, ρ the fluid density, and v the kinematic viscosity.

To solve these equations, two different methodologies were employed: the Reynolds Average (RANS) approach and the Large Eddy Simulations (LES).

2.1. Reynolds average Navier Stokes

The Reynolds-averaged approach is based on decomposing the velocity as $\mathbf{u} = \overline{\mathbf{u}} + \mathbf{u}'$ where $\overline{\mathbf{u}}$ is the average velocity vector and $\mathbf{u}'$ the velocity vector fluctuation. The average continuity and momentum equation (RANS), for a steady state incompressible flow has the same form of the Navier–Stokes equation, with an additional term which is the divergence of the turbulent Reynolds stress term, $\nabla \cdot (\overline{\mathbf{u}'\,\mathbf{u}'})$. This term represents the influence of the fluctuation on the average flow. In order to close the set of average equations, the turbulent Reynolds stress must be determined. It can be modeled based on the Boussinesq hypothesis, where the turbulent stress ($\overline{\mathbf{u}'\,\mathbf{u}'}$) is obtained through an analogy with Stokes law, i.e., the anisotropic part of the stress tensor $\mathbf{a}$ is proportional to the deformation rate, $\mathbf{S}$

$$-\overline{\mathbf{u}'\,\mathbf{u}'} = \mathbf{a} - (2/3)\;k\;\mathbf{I};\;\mathbf{a} = v_t\,2\,\mathbf{S}\,;$$
$$\mathbf{S} = 0.5(\nabla\;\overline{\mathbf{u}} + \nabla\;\overline{\mathbf{u}}^{\mathrm{T}});\;\;k = \mathrm{tr}(\overline{\mathbf{u}'\,\mathbf{u}'}), \tag{2}$$

where k is the turbulent kinetic energy, $\mathbf{I}$ is the identity tensor, and v_t is the turbulence viscosity, which is the final goal of the RANS modeling and the only parameter related to the turbulence action to directly alter the momentum transport. Alternatively to the Boussinesq hypothesis, $\overline{\mathbf{u}'\,\mathbf{u}'}$ can be directly determined through the solution of a set of transport equations, as is the case for the Reynolds stress model (RSM).

The turbulence models investigated here present different levels of complexity. The first one is the Spalart–Allmaras model (SA), which is a one equation model. Developed by Spalart and Allmaras (1992), this is a relatively simple model that solves a transport differential equation for the turbulent viscosity and, therefore, it requires smaller computational effort. The Spalart–Allmaras model was designed specifically for aerospace applications involving wall-bounded flows and adverse pressure gradients. Since the Reynolds tensor's trace can be incorporated in a modified pressure, only the anisotropic part of the Reynolds stress is relevant for the transport of momentum. The Spalart–Allmaras model takes advantage of this fact and proposes a transport equation for the turbulent viscosity v_t, without trying to predict the turbulent kinetic energy.

Three versions of the $k - \omega$ SST model were investigated: $k - \omega$ SST (SST), and two variations of transition SST model: (i) transition SST model (SST tran) of Fluent and (ii) transition SST specified intermittence (SST SI) of CFX.

The shear–stress transport (SST) $k - \omega$ model (Menter, 1994), is a two-equation model, and it was proposed for aeronautical flow simulations with strong adverse pressure gradients and separations, by combining the best virtues of both $k - \varepsilon$ and $k - \omega$ models. For boundary layer flows, the $k - \omega$ model is superior to the $k - \varepsilon$ model in the solution of the viscous near-wall region, and has been successfully employed in problems involving adverse pressure gradients. Nevertheless, it requires a non-zero boundary condition on ω even for non-turbulent free-stream, and the calculated flow is very sensitive to the specified value (Menter, 1994). On the other hand, it has also been shown (Cazalbou et al., 1993) that the $k - \varepsilon$ model does not suffer this deficiency.

The SST model blends the robust and precise formulation of the $k - \omega$ model near the walls with the free-stream independence of the $k - \varepsilon$ model outside the boundary layer. To accomplish this, the transport equation for ε in the $k - \varepsilon$ model is written in terms of ω instead. Then the standard $k - \omega$ model and the transformed $k - \varepsilon$ model are both multiplied by a blending function and added together. This blending function F_1 is zero at the inner region of a turbulent boundary layer, leading to the standard $k - \omega$, and tends to a unitary value (corresponding to the standard $k - \varepsilon$ model) at the outer region of the boundary layer.

The two tested versions of the transition SST model (Menter et al., 2006) are based on the $k - \omega$ SST, with complimentary transport equations to capture transition. The first model (SST trans) is readily available in Fluent and requires the solution of two additional equations, one for the intermittence and one for the momentum thickness. The second variant is the SST SI available in CFX, which requires the solution of only one equation for the intermittency, using a specified constant value for the transition onset momentum thickness Reynolds number.

2.2. Large eddy simulation

In the large eddy simulation (LES) approach a spatial filter is applied to the transport equations (Navier–Stokes and continuity) in order to separate the small from the large eddies (or scales). The filter operation is here done implicitly, or embedded in the finite volume method, through the control volume integral of each term in the equation. The result of this operation is that almost all terms can be reinterpreted as operands on filtered version of variables instead of operands on the original variables. The exception is the advective term, for which the filter operator does not commute with the product operator, or $\overline{\mathbf{u}\,\mathbf{u}} \neq \overline{\mathbf{u}}\,\overline{\mathbf{u}}$. Here, $\overline{()}$ denotes a spatially filtered quantity, in this case, either the velocity field or the product of two velocities. Aiming to solve equations for filtered quantity, such as filtered velocity, the advection term in Navier–Stokes equation will be replaced by $\nabla \cdot (\overline{\mathbf{u}}\,\overline{\mathbf{u}} + \overline{\mathbf{u}\,\mathbf{u}} - \overline{\mathbf{u}}\,\overline{\mathbf{u}})$ or $\nabla \cdot (\overline{\mathbf{u}}\,\overline{\mathbf{u}}) + \nabla \cdot \boldsymbol{\tau}_{\mathrm{SGS}}$ where $\boldsymbol{\tau}_{\mathrm{SGS}} = \overline{\mathbf{u}\,\mathbf{u}} - \overline{\mathbf{u}}\,\overline{\mathbf{u}}$ represents the subgrid tensor divided by the fluid density, which can also be interpreted as the commutative error in the product and filtering operation. The divergent of this subgrid tensor must therefore be added to the transport equation for the filtered variables (a filtered version of Navier–Stokes equation). A closed expression for this term cannot be found and hence it must be separately modeled. In this investigation, $\boldsymbol{\tau}_{\mathrm{SGS}}$ is also modeled based on the Boussinesq hypothesis as follows:

$$\tau_{\mathrm{SGS}_{ij}} = -2\,\overline{\overline{S}}_{ij}\,v_{SM} + \frac{2}{3}\left(\overline{\overline{u_k''\,u_k''}}\right)\delta_{ij} \quad ; \quad \overline{\overline{S}}_{ij} = \frac{1}{2}\left(\frac{\partial \overline{\overline{u_i}}}{\partial x_j} + \frac{\partial \overline{\overline{u_j}}}{\partial x_i}\right) \tag{3}$$

where v_{SM} is the turbulent subgrid viscosity, which was modeled with the Dynamic Smagorinsk subgrid model (Germano et al., 1991; Lilly, 1992), and $\overline{\overline{S}}_{ij}$ is the filtered deformation rate.

The dynamic Smagorinsk subgrid viscosity model is based on the Smagorinsly–Lilly model (Germano et al., 1991; Lilly, 1992),

where the sub-grid eddy-viscosity is as follows:

$$\upsilon_{SM} = (L_s)^2 \sqrt{2\overline{\overline{S}}_{ij}\,\overline{\overline{S}}_{ij}} \quad ; \quad L_s = \min(k_v\,d\,,\,C_s\,\forall^{1/3}) \tag{4}$$

where L_s is the mixing length for subgrid scales, and k_v is the von Kármán constant, d is the distance to the closest wall, C_s is the Smagorinsky constant and $\forall$ is the volume of the computational cell. In the dynamic approach, the Smagorinsky constant C_s is dynamically computed based on the information provided by the resolved scales of motion. Although, C_s can vary in time and space, to avoid instability it was clipped at zero and 0.23.

3. Test case

The test case chosen for this investigation is the incompressible aerodynamic flow around a thin flat plate, exactly as the one employed in the experiments of Crompton (2001). The sharp leading edge is beveled at 20° (Fig. 2), with $c=160$ mm as chord length and 6 mm of thickness. For the LES case, the domain span was defined as $b=c/4$, based on a previous study (Sampaio, 2006) which showed no significant velocity correlations for distances larger than that. Because of the expected homogeneity in the spanwise direction (z axis), a 3D RANS simulation would not improve the predictions, therefore two-dimensional domain, with spanwise width equal to one, was defined for the RANS simulations.

As mentioned before, the flow around this flat plate presents basically the same features at a wide range of Angle of Attacks (AOA). The pressure coefficient over the top surface, for instance, collapses for AOA between 1° and 5°, when the distance over the plate is normalized by the reattachment length. Thus, this paper concentrates on the 1° AOA case, because of the extensive data available from experiments (Crompton, 2001).

All numerical simulations performed in this paper used the same chord-based Reynolds number ($\mathbf{Re}_c = U_\infty c/\upsilon$) chosen by Crompton (2001), $\mathbf{Re}_c = 2.13 \times 10^5$.

Fig. 2 shows the plane computational domain used in simulations, which was defined based on the work of Collie et al. (2008). Previous studies (Rezende, 2009) provided evidence that the computational domain is large enough to guarantee solution independence, while still suitable in terms of mesh size and stretching/shrinking rate.

In the same Fig. 2, the boundaries of the domain are shown with the corresponding conditions imposed during the numerical

Fig. 2. Computational domain.

simulations. Left and bottom boundaries were defined as "Inlet", while upper and right boundaries were defined as "Outlet".

At the inlet boundaries a uniform fixed velocity was prescribed, with a 1° angle relative to the horizontal, which provided the desired angle of attack of the plate. The turbulence intensity of the freestream, defined as $\varsigma = (1/3)(\overline{u'u'}+\overline{v'v'}+\overline{w'w'})/U_\infty^2 = (2/3)\,k/U_\infty^2$, was set as 0.05%, as measured in wind tunnel (Crompton, 2001). The freestream turbulence intensity at the inlet does not influence the flow, since the generation of turbulence at the plate edge is very high. The same numerical solution was obtained by varying ς from 0.001% to 1%. For the transition models, intermittency equal to 1 was prescribed at the inlet. The influence of the inlet intermittence was also investigated, and it was observed that a variation from 0.1 to 1 did not affect the result. Constant pressure equal to the freestream p_∞ was set at the outlet boundaries. Non-slip conditions were imposed over all plate surfaces. For the 3-D LES simulation, a periodic boundary condition at front and back domain borders was imposed.

4. Numerical details and discretization

The flow field was determined with the commercial softwares Fluent (2013) and CFX (2013) both from ANSYS. The turbulence models Spalart–Allmaras (SA), $k-\omega$ SST (SST and one version of the transition $\kappa-\omega$ SST) were solved with Fluent, while the other transition $\kappa-\omega$ SST was obtained with CFX. The LES case was simulated with Fluent (2013). Both codes are based on the finite volume method. Second order spatial discretization scheme were selected. QUICK (quadratic upwind) interpolation scheme was chosen for all Fluent RANS simulations, while "High Resolution" (blending upwind and central difference) was specified for the CFX runs. The pressure-velocity coupling was handled by the SIMPLE algorithm. LES simulations were obtained with Central Difference spatial discretization and second order implicit time discretization. The pressure–velocity coupling was handled by the PISO algorithm. The problem was considered converged when the maximum residue of all equations was smaller than 10^{-6}.

The mesh was created in the software GAMBIT. The smallest mesh size tested had a slightly larger number of points than the one employed by Collie et al. (2008). A mesh validation was performed to guarantee that the discretization errors were negligible and did not affect the conclusions drawn about the turbulence models performance. Three mesh sizes were selected to be presented here: 150×10^3 nodes; 330×10^3 nodes and 600×10^3 nodes. The mesh size was increased in the axial direction and vertical direction in a proportional rate. The maximum mesh expansion rate was kept below 1% in the region around the plate, while in the rest of the computational domain, away from the plate, a value of 5% was allowed. The distance of first node above the plate was defined as to guarantee y^+ smaller than 1, as recommended for SST models. Fig. 3 illustrates the mesh distribution in the whole domain and details near the plate and plate tip.

To help analyze the mesh quality; the dimensionless pressure and viscous force contributions over the upper surface of plate were determined. The vertical pressure force contribution F_p and
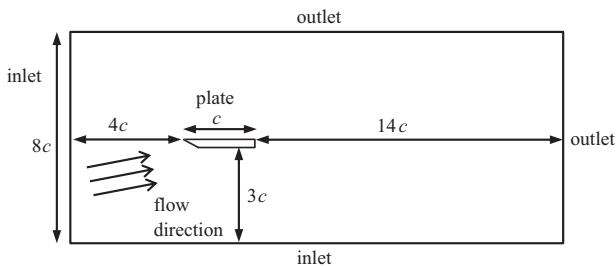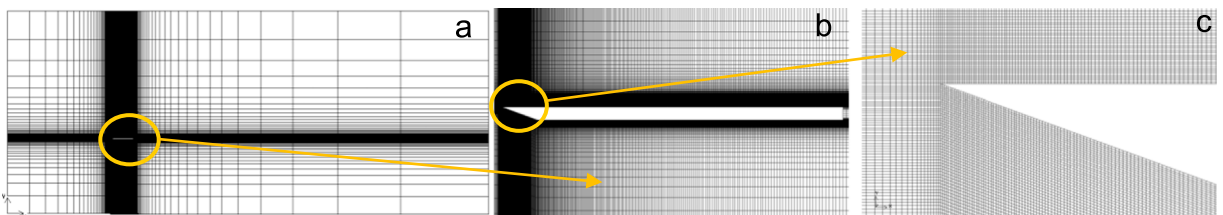
Fig. 3. Mesh distribution. (a) Full domain, (b) plate, and (c) plate tip.

axial viscous force contribution F_τ were normalized as follows:

$$C_L = \frac{F_p/(c\,b)}{0.5\,\rho\,U_\infty^2}; \quad C_D = \frac{F_\tau/(c\,b)}{0.5\,\rho\,U_\infty^2} \tag{5}$$

Fig. 4a shows the lift coefficient C_L obtained with the three selected meshes used in the RANS validation study, while Fig. 4b shows the drag force C_D obtained with the same meshes. The mesh validation test was run for all models. The lift coefficient was less sensitive to the mesh refinement than the drag coefficient. This behavior is expected since the drag coefficient is very small, leading to larger relative differences. The corresponding C_L differences between the finest mesh were: SA: 0.9%; SST: 0.1%, SST tran: 0.6%, SST SI: 7%. For C_D, the differences were: SA: 1.6%; SST: 1.2%, SST trans: 4.0%, SST SI: 10%.

All meshes kept y^+ values below unity, meaning that all models resolve the boundary layer to the wall. Since the differences in C_L and C_D between the finest meshes were small, the intermediate mesh of 600×10^3 was selected for the present analysis.

For all cases examined, the reattachment point difference between the coarse and intermediate mesh was less than to 3%, while from the intermediate to the fine mesh, it was less than to 1%, with the exception of the SST Transition, which maintains practically the same difference (2.8%).

From this mesh validation study, the intermediate mesh (330×10^3 nodes) was considered the most suitable one, as it is fine enough to guarantee grid independence yet not too large to allow short simulations time.

With respect to the LES case 16 uniformly distributed points were employed in the spanwise direction. The same mesh size selected for the RANS simulations were employed in the x–y plane. The lift and drag coefficient predicted with LES were $C_L = 0.139$ and $C_D = 1.97 \times 10^{-3}$. All RANS models super estimated both coefficients in relation with LES prediction's.

Table 1 presents the maximum and average y^+ at the first nodal point along the plate, corresponding to the selected mesh. It can be seen that all RANS turbulence models predicted a similar y^+ distribution, with average value equal to 0.3 and maximum value inferior to 0.9. The y^+ distribution obtained with LES was slightly higher. The average value was equal to 0.756, and maximum value equal to 1.39, with only 13% of the points over the plate above 1.

5. Results

The results obtained in the present work with the selected RANS and LES (Germano et al., 1991; Lilly,1992) models are compared to the experimental data of Crompton (2001).

Initially, time average data of the fields of interest is presented, followed by the second order statistics.

5.1. Average velocity field

The reattachment points x_r obtained with each model are presented in Table 2, where the results from Collie et al. (2008) for the $k-\omega$ and $k-\omega$ SST models are also shown. Table 2 shows that the best prediction for x_r was obtained with LES, followed by SA, while Collie's result with SST is better than those predicted in this work. Both transition models predicted the reattachment with equivalent absolute error, however the SST trans underestimates its value, while the SSI SI overestimates.

At the present work, the mesh was defined based on rigorous grid test, in which the final one was found to present approximately three times more elements than the one employed by Collie et al. (2008). To identify the cause of the discrepancies between Collie's work and the present one, an additional test was performed, using the same model (SST), the same mesh, and a lower order scheme for spatial discretization. The influence of the discretization scheme was investigated, solving the problem with the *Power-Law* scheme. The reattachment point obtained as 0.144 (2.86%), indicating a better agreement in the prediction value of x_r, relatively to the higher order QUICK scheme. However, this result is misleading, as in fact it indicates that the SST model does not provide the appropriate diffusion for this flow. By introducing an artificial diffusion with the low-order model, a better prediction of the size of the recirculation bubble obtained. The better result obtained by Collie et al. (2008) for x_r in a coarser mesh – and consequently more prone to spurious numerical diffusion – corroborates this hypothesis.

Table 1
Maximum and average y^+ of the first internal node along plate.

	SA	SST	SST trans	SST SI	LES
$y_{\mathbf{max}}^+$	0.884	0.870	0.888	0.802	1.39
y_{mean}^+	0.283	0.250	0.295	0.293	0.756

Table 2
Reattachment point.

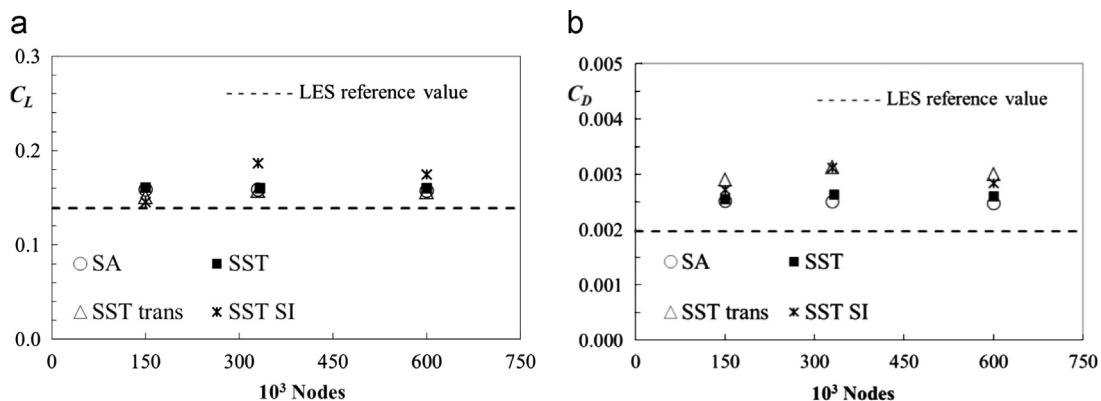| Model	Exp	SA	SST	SST trans	SST SI	$k-\omega$ [a]	SST [a]	LES
x_r/c	0.140	0.146	0.166	0.124	0.162	0.184	0.149	0.141
Error (%)		4.61	18.4	−11.4	13.3	24	5.8	0.64

[a] Collie et al. (2008).

Fig. 4. Pressure and friction coefficient. Mesh independence test. (a) Lift coefficient and (b) drag coefficient.

Although the reattachment point prediction is an important parameter to evaluate a turbulence model, it cannot be the determinant of the merits of each model, and other flow features must be considered as well. For instance, on the preliminary tests with the Reynolds stress model (RSM) model, excellent prediction of the reattachment point was obtained, with only 2.5% deviation. However, it has an unacceptable anomaly in the resulting stream-lines, which bends back to the reattachment point, reflecting in poor quality of prediction of all other variables. This spurious result has already been observed by several authors, such as Hanjalic and Jakirlic (1998), when examining the backstep flow case with the RSM model.

Fig. 5 presents the streamlines obtained with $k-\omega$ SST (SST) and LES close to the leading edge, in the region of the main recirculation bubble. It can be verified in Fig. 5a that SST model was not able to predict the secondary recirculation bubble, which is observed experimentally. The absence of the secondary bubble in the RANS predictions is directly related to the overprediction of the turbulence by those simulations, inducing the flow inside the bubble to be more resistant to the secondary separation, keeping the reverse boundary layer attached to the plate inside the main bubble.

Fig. 5b shows that the secondary recirculating bubble, inside the main bubble, was predicted with LES. After the reattachment point and flowing upstream, a new turbulent boundary layer adjacent the upper surface of the plate is formed. This boundary layer undergoes a process of relaminarization due to an existing favorable pressure gradient between the reattachment point and the low pressure zone in the bubble central region. However, due to an adverse pressure gradient between the beveled edge and the minimum pressure peak, the boundary layer suffers an opposing forcing leading to a new separation, forming the secondary bubble. The higher the relaminarization intensity is, the greater the chances of a secondary boundary layer separation (second bubble), and this process will take place closer to the leading edge.

The velocity profiles and turbulent quantities (second-order statistics) within the boundary layer were obtained in experiments carried out by Crompton (2001) in nine different stations located on the plate, as shown in Fig. 6. Crompton (2001) has also provided information regarding the distribution of pressure over the plate. The results obtained with the different simulations are compared with the experimental data at these stations.

The chordwise mean velocity profile is plotted against the normal distance from the plate, y, in Fig. 7 at six stations for all turbulence models. The experimental data is included to allow comparison. For $\alpha=1^0$ only the first two stations are contained within the length of reattachment, as shown in Fig. 6. To allow a clearer visualization of the differences in results for the five tested models, a log scale was employed in the graphs. The values of u and y have been normalized by the free-stream velocity, U_∞ and the chord, c, respectively. The log scaling idea is borrowed from the traditional boundary layer analysis, in which u^+ is plotted against y^+ in logarithmic scale, producing a straight line in the inertial range. Unfortunately, however, the wall shear stress was not available, nor could be inferred from the experimental data. Therefore, it was not possible to get the velocity and distance values in wall units. Notwithstanding, employing the log scale on y/c brings two benefits: it amplifies the region of interest (close to the wall) relatively to the inertial range and outer region of the boundary layer, which would otherwise mask the former; and it would still produce a straight line in the regions where an inertial range is expected.

In Fig. 7, the first two stations (Fig. 7a and b) are inside the recirculation zone for all turbulent models but the "SST trans". Due to the strong influence of this region, which reflected by the curvature of the streamlines, a linear behavior in the log scale, normally found in a regular boundary layer, is not expected in these two stations. For the first station (Fig. 7a) it is also evident that, when compared to the experimental data, all RANS models predicted a higher velocity magnitude in the near wall region and a thinner laminar viscous sublayer, whose frontier coincides with the change in the curve trend in the semi-log plot as one departs from the wall. As expected, LES results are in better agreement with the experimental data, providing a good prediction for all different regions, from the viscous sublayer to the outer flow.

The RANS turbulence models predicted a laminar sublayer thickness in the range $5 \times 10^{-4} \sim 10^{-3}$, while experiments point to 5×10^{-3}. This means that a higher gradient and, therefore, a higher wall shear stress, was predicted by all models. In this respect, the turbulence models "SA" and "SST trans" were the two
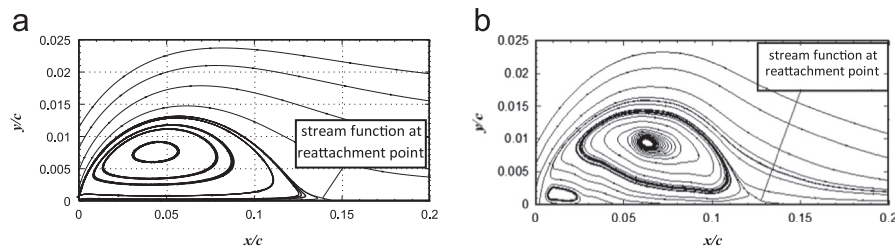
Fig. 5. Streamlines near flat plate tip. (a) SST and (b)LES.

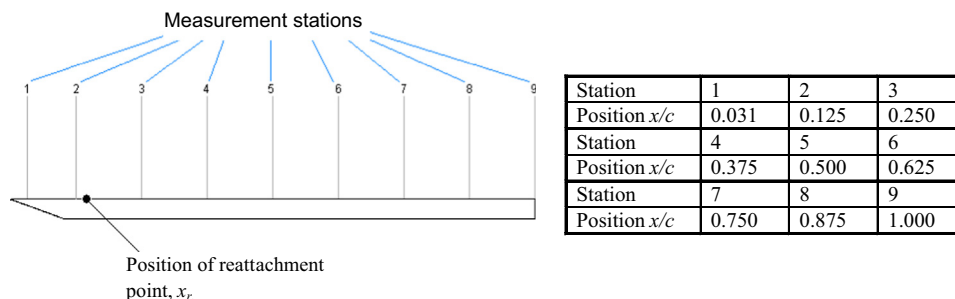| Station	1	2	3
Position x/c	0.031	0.125	0.250
Station	4	5	6
Position x/c	0.375	0.500	0.625
Station	7	8	9
Position x/c	0.750	0.875	1.000

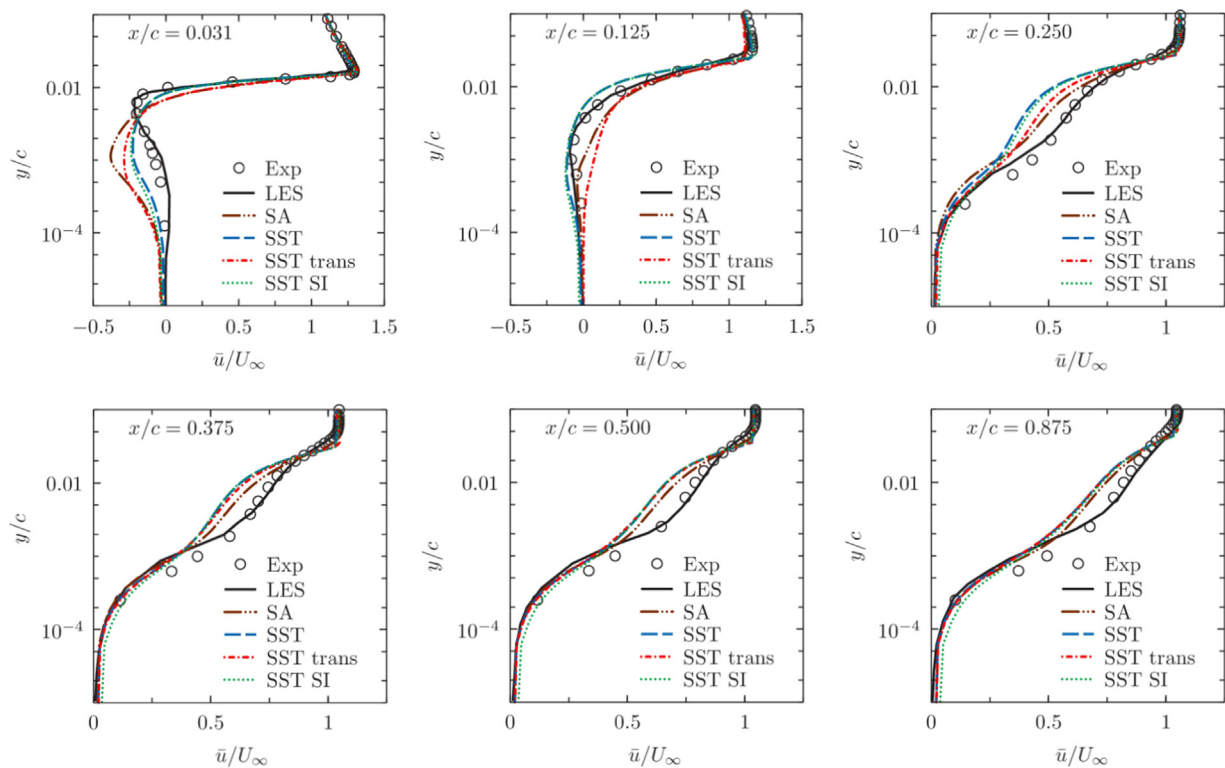**Fig. 6.** Measurement stations and position of reattachment point.

Fig. 7. Dimensionless mean velocity along vertical coordinate at several stations. (a) $x/c=0.031$, (b) $x/c=0.125$, (c) $x/c=0.250$, (d) $x/c=0.375$, (e) $x/c=0.500$, and (f) $x/c=0.875$.

furthest from the experimental data. There were no noticeable differences in the "SST" and "SST SI" results for this first station, and they were more accurate not only in the aforementioned region, but also in the shear layer that separates the recirculation zone from the external flow. The "SA" and "SST trans" models overpredicted the wall shear and underpredicted the outer bubble shear layer, which can be related to the shorter reattachment length results.

In Fig. 7b, the inaccuracies in the reattachment length were visible for the "SST trans" model, as no reverse flow was noticed in this position (Station 2, at $x/c=0.125$). This means that this station is already outside the predicted recirculation bubble, which did not happen with the other models. In this respect, the "SA" model also presented a weaker reverse flow, which is in accordance to its shorter reattachment length. In this same figure, one can observe that the external flow (outside the bubble, for $y/c > 0.03$) was very accurately captured by the "SST" and "SST SI" models, while the other two did not captured the velocity peak value (around 1.2).

As the flow develops over the plate, the different models results become closer, to the point where in Fig. 7f the disagreement in $\bar{u}/U_\infty$ is not larger than 0.1 everywhere. In comparison to experimental data, however, all models presented a discrepancy of about 0.3 or more, with the "SA" model being marginally superior in this respect.

For all stations located outside the recirculation bubble (Fig. 7c–e), one can notice a linear dependence of $\bar{u}$ with y in the near wall region (up to around $y/c=10^{-3}$), which appears in the graphs as an exponential shape because of the log scaling. This corresponds to the viscous sublayer, in which the viscous forces are predominant over the inertial ones. Despite the inaccuracies in capturing the right velocities, the extension of this subrange was fairly accurate for all models in this development zone, ranging from $y/c \approx 10^{-3}$ at $x/c=0.250$, to $y/c \approx 2 \times 10^{-3}$ at $x/c=0.875$, in a subtle monotonic increase. The above estimate is based on the inflection point in the curves, which technically pertains to the buffer layer rather than to the laminar sublayer. Although this procedure is not precise, it does give a good idea of the growth of the sublayer. The same conclusions can be

drawn for the inertial range of the boundary layer, i.e., the extension of this layer increases monotonically as the flow develops. Initially (at $x/c=0.250$) the inertial subrange extends from 0.001 to 0.004, while near the end of the plate (at $x/c=0.875$), it extends from 0.002 to 0.015. It can also be seen that the normalized velocity profile is almost the same at stations larger than $x/c=0.5$, which corresponds to the boundary layer developing regions, after reattachment.

Overall, LES results were in much better agreement with experiments, which was expected from a methodology that was conceived to capture most of the spectrum energy. There is, however, some level of disagreement, mostly visible after reattachment. As it was the case with all RANS models, a small mistake in capturing the reattachment length resulted in difficulties to match the stage of development of the new boundary layer that is formed after reattachment point, when comparing LES to experimental data. However, in RANS cases, this earlier or later boundary layer beginning is still to be added to other important source of errors. It is worthy to note that some of these errors are intrinsic to the Boussinesq hypothesis, and cannot be eliminated, unless more complex representations for the Reynolds stress tensors are evoked. On the other hand, in LES, these other source of errors are minimized as long as a fine mesh is employed, even for those models that employ the Boussinesq hypothesis for the subgrid stress tensor.

Regarding Fig.7b, one can notice that LES accurately captured the negative velocity. However, the anticipation of the reattachment, as presented in Table 2, resulted in an advance in the profile development that can be seen in the next stations (Fig.7c–f).

5.2. Pressure and friction coefficient

The pressure and friction coefficients are defined in Eq. (6), and their distribution over the plate, obtained with the different models can be seen in Figs. 8 and 9, respectively. In these figures, only the first 20% of the plate length was shown, since after this
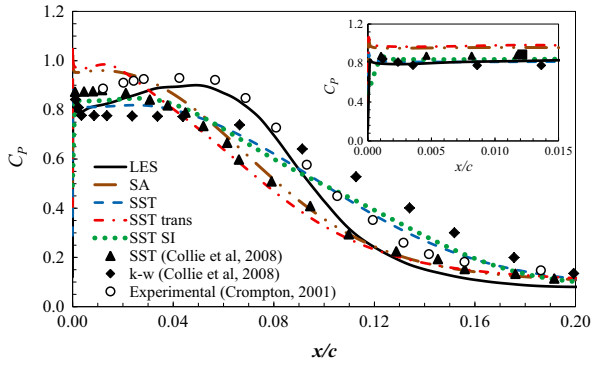
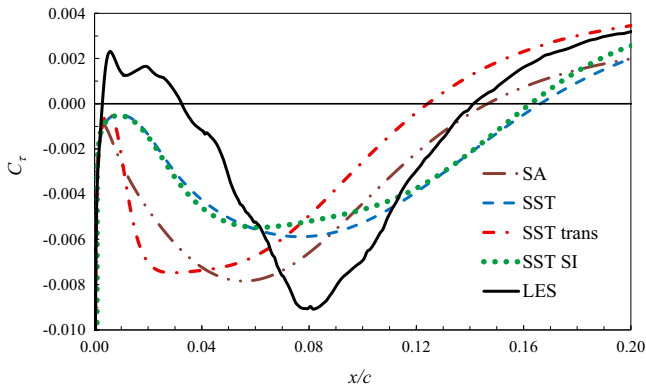Fig. 8. Pressure coefficient along the plate.

Fig. 9. Friction coefficient along the plate.

coordinate, pressure and friction are almost constant and coincident with the experimental data. The disagreement between the RANS predictions is only observed in the recirculation region near the plate tip. However, an excellent agreement of LES results with experimental data was obtained in the same region.

$$C_p = \frac{p_\infty - \overline{p}}{0.5\,\rho\,U_\infty^2}; \quad C_\tau = \frac{\tau_w}{0.5\,\rho\,U_\infty^2} \qquad (6)$$

The pressure distributions obtained with the tested models are also compared, in Fig. 8, with the prediction of Collie et al. (2008) employing the $k-\omega$ and SST models. Analyzing Fig. 8, a visible suction can also be seen inside the bubble region, in the upper side of the plate, followed by a significant increase in the pressure coefficient, indicating a pressure drop. The intense pressure peak at $x/c=0$ (Fig. 8) predicted by all models is not present in Crompton's data (2001), possibly due to spatial resolution of the experiment. Crompton measured a smoother peak in pressure at $x/c=0.05$, indicating the presence of a suction within the bubble region. After the reattachments point ($x/c>0.2$), the pressure is approximately constant, and it is well predicted by all models.

None of the selected RANS models were able to capture the correct formation of the recirculation zone, which presents a visible secondary suction within this region. Of all the models tested, the most accurate in this respect was SST, followed by SST SI. The Spalart Allmaras model (SA) and the transition SST of Fluent (SST trans) were able to predict the peak level, but with a faster pressure recovery, which should instead be sustained in the recirculating region, according to the experimental result. All RANS models predicted smaller suction due to the inexistence of the secondary bubble, inducing these models to anticipate the pressure recovery. Excellent agreement was obtained between LES prediction and the experimental data. The failure to correctly determine the pressure distribution is due to the inability of turbulence RANS models to predict the exact transition location
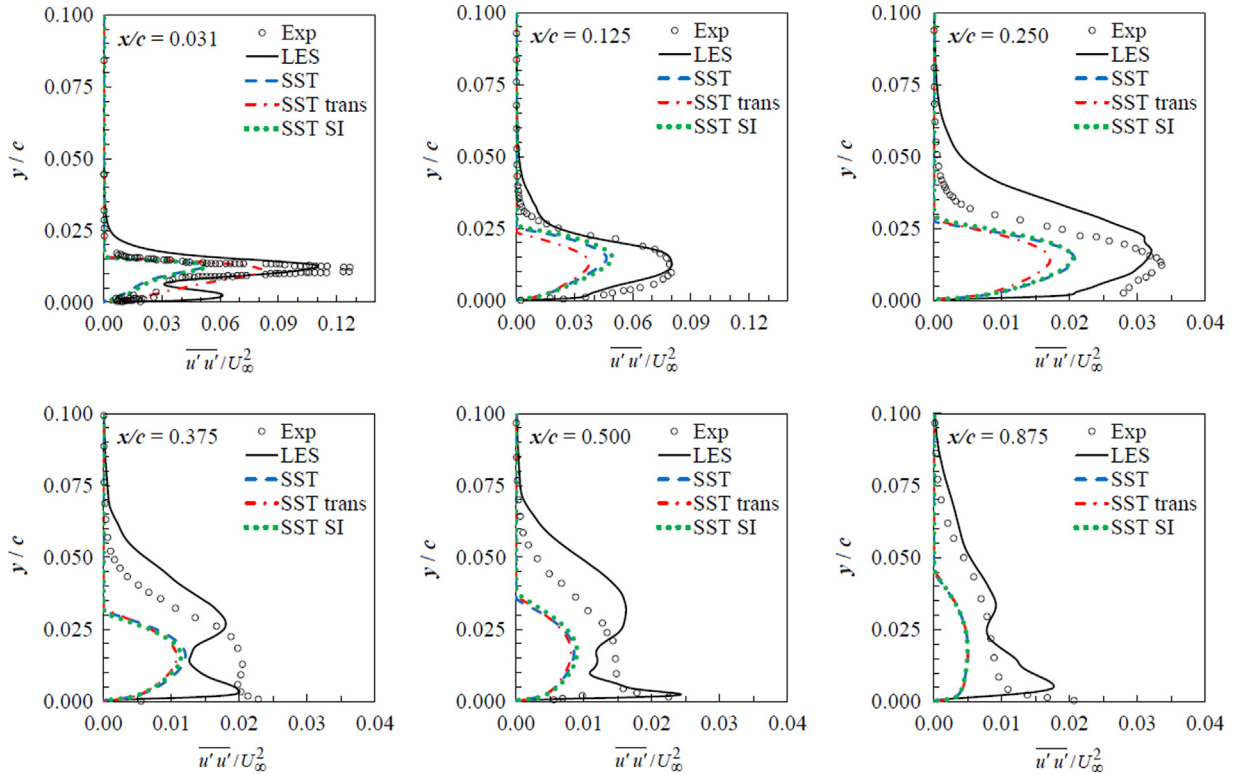
Fig. 10. Second order statistics $\overline{u'u'}/U_\infty^2$. (a) $x/c=0.031$, (b) $x/c=0.125$, (c) $x/c=0.250$, (d) $x/c=0.375$, (e) $x/c=0.500$, and (f) $x/c=0.875$.

and the existence of the secondary recirculation region. The transition SST models were also not capable of adequately predicting the pressure in the suction region, and showed a similar behavior to the $\kappa-\omega$ and SA models, despite their higher complexity.

The difference between Collie et al. (2008) $k-\omega$ SST prediction and the one obtained in the present work can be attributed, as already mentioned, to numerical error, due to a coarser mesh employed by Collie et al. (2008).

These results are consistent with the trend shown by the velocity profiles in Fig. 7: the higher velocities near the wall in the region of the bubble, predicted by all turbulence models, are closely related to the larger pressure drop experienced in this region. Moreover, it is interesting to note that shorter bubbles, as in SST trans and SA models, means that the average radius of the recirculation bubble is smaller and that the pressure gradients must be stronger to provide the necessary centripetal forces. And in fact, one can verify that pressure suctions are higher for these two models.

The friction coefficient distribution is shown in Fig. 9. The coordinate where C_τ is equal to zero corresponds to the reattachment point. A strong C_τ variation near the tip with shear reduction can be seen. However, this variation was not sufficiently strong to cause the formation of the secondary bubble with the RANS models, while the existence of the secondary bubble can be clearly seen in the LES results. The shear profile is directly connected to the pressure distribution, where SA and SST trans presented the worst predictions, with sharp friction drop associated with sharp pressure recovery. All other RANS models presented similar results.

5.3. Second order statistics

The correct prediction of the second order statistics is essential for the determination of the flow characteristics, especially when separation is imminent. Fig. 10 present a comparison of $\overline{u'u'}/U_\infty^2$ obtained with the several RANS models, with LES and with the experimental data (Crompton, 2001) at the different stations. Figs. 10a–b correspond to the stations within the recirculating bubble, and Fig. 10c–f after the reattachment point. Near the leading edge (Fig. 10a), RANS models were able to predict the $\overline{u'u'}/U_\infty^2$ peak position, but its value was underestimated. As one moves downstream, a diffusion of $\overline{u'u'}/U_\infty^2$ can be observed, and although the peak is smaller, the vertical profile of $\overline{u'u'}/U_\infty^2$ is very similar up to the one at $x/c=0.250$. Further downstream (Fig. 10d–f), there is an increase in the $\overline{u'u'}/U_\infty^2$ values very close to the wall, which the RANS models did not capture. A much better prediction was obtained with the LES formulation. Note that the results from SA model are not plotted in Fig. 10. This is due to the fact it directly models the deviatoric part of the turbulent tensor, without estimating its trace or its diagonal elements.

The profiles along the vertical directions of the dimensionless normal components of the deviatoric anisotropic stress a_{xx}/U_∞^2 are shown in Fig. 11 for four stations. In Fig. 12, the results obtained with k-ω SST and LES for a_{xx}/U_∞^2 are compared with a_{yy}/U_∞^2. Fig. 13
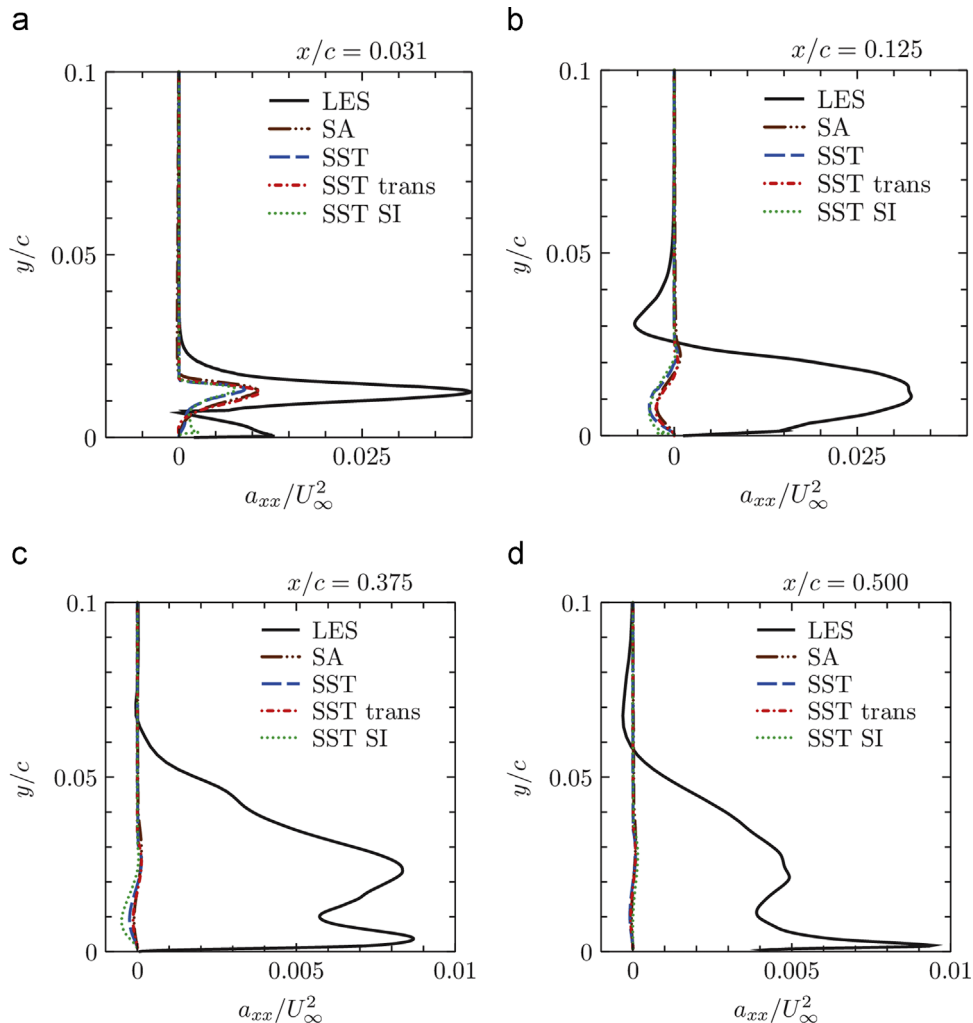

Fig. 11. Normal component of the deviatoric anisotropic tensor, a_{xx}/U_∞^2. (a) $x/c=0.031$, (b) $x/c=0.125$, (c) $x/c=0.375$, and (d) $x/c=0.500$.
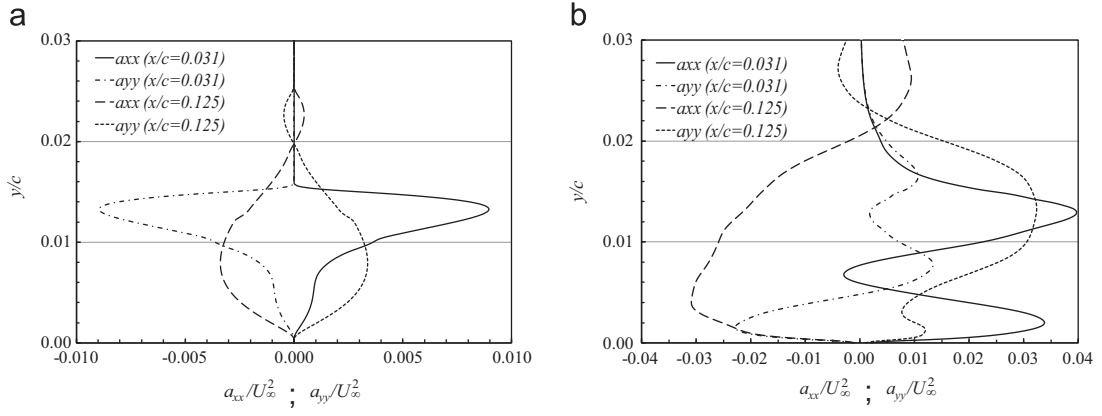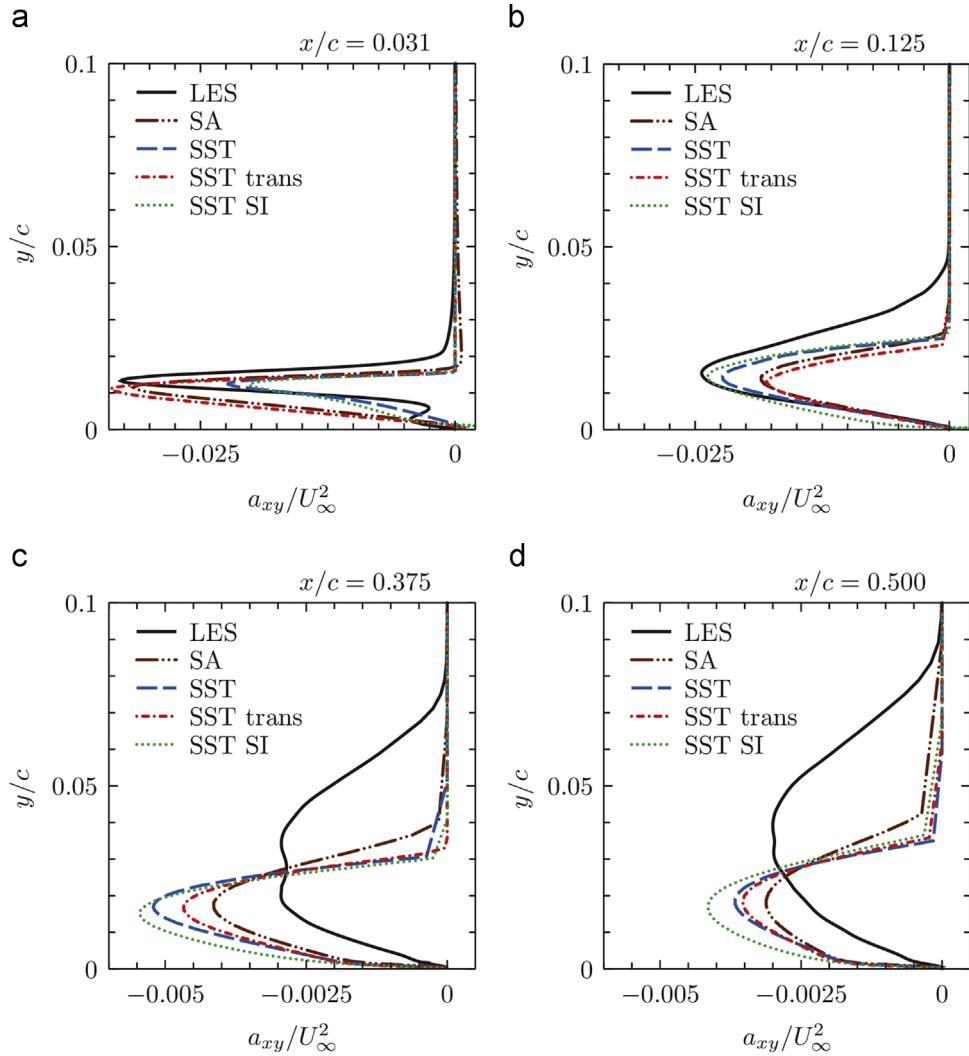
Fig. 12. Normal components of the deviatoric anisotropic tensor, a_{xx}/U_∞^2; a_{yy}/U_∞^2. (a) SST and (b) LES.

Fig. 13. Shear component of the deviatoric anisotropic tensor, a_{xy}/U_∞^2. (a) x/c=0.031, (b) x/c=0.125, (c) x/c=0.375, and (d) x/c=0.500.

presents the shear component a_{xy}/U_∞^2. Examining Fig. 11a (inside the bubble), it can be seen that although all models underpredicted its peak, its position was correctly captured. Only the SST SI model was able to predict the second peak close to the wall, although it was much smaller than the LES result. This peak might be related to the presence of the secondary bubble. Moving

downstream, LES predicted an increase in the secondary peak, creating a region of negative a_{xx}/U_∞^2 (Fig. 11b). The agreement of the RANS models with LES is very poor, with the reverse peak captured by the RANS models shifted closer to the wall. It can also be seen that the normal deviatoric anisotropic tensor of all RANS models rapidly decays. After the reattachment point, due to the

boundary layer development, there is a slower decrease of a_{xx}/U_∞^2 near the wall, leading to two peaks at $x/c = 0.375$, as it can be seen with the LES prediction (Fig. 11c). As one moves farther from the leading edge (Fig. 11d), the a_{xx}/U_∞^2 far from the wall is damped, resulting in a peak of a_{xx}/U_∞^2 at the wall.

The normal components of the deviatoric anisotropic tensor, a_{xx}/U_∞^2 and a_{yy}/U_∞^2 obtained with SST model are presented in Fig. 12a, where it can be seen a perfect symmetry of the tensor components. This was expected as the Boussinesq hypothesis models the anisotropy part of the Reynolds stress as being aligned with the symmetric part of the velocity gradient, whose trace is null, which in 2D means that $a_{xx} = -a_{yy}$. All RANS models presented similar results. A significantly different solution was obtained with LES (Fig. 12b). Higher values of the deviatoric anisotropic stress were obtained, and the flow anisotropy can be clearly seen.

Analyzing the shear component of the deviatoric anisotropic tensor in Fig. 13, one can note that inside the recirculating bubble, RANS and LES predictions are similar. After the reattachment point, RANS models simply damp a_{xy}/U_∞^2, maintaining the peak position, while LES results show a spread of a_{xy}/U_∞^2, shifting its peak away from the wall.

The next figures (Figs. 14–16) are intended to show where and how the SST model fails to correctly capture the effect of the turbulent Reynolds stress tensor on the momentum equation. The reference used for this assessment is the large eddy simulation data, where the turbulent forcing ($f = \nabla \cdot \tau_{SGS}$) is calculated as a time average of the second moment fluctuations of the resolved field, $\tau_{SGS} = \overline{(\mathbf{u}' \mathbf{u}')}$. This quantity is assumed to be complete, in the sense that it contains most of the turbulent energy of the flow at each point in space, therefore neglecting the subgrid turbulence. The magnitude of this force field obtained from LES is shown in Fig. 14a, for a region surrounding the plate leading edge. Notice the most intense forces happen in the neighborhood of the shear layer of both primary and secondary separation, indicated by dash lines. Fig. 14b shows the component of this force that is aligned with the mean velocity. It is very clear that, for the main recirculation, there is an inversion of the force direction across the shear layer, which was expected, as the outer flow tends to lose energy and accelerate the inner bubble flow, while the latter decelerates the former. In Fig. 14c, the force results from SST model show a more defined and

abrupt transition outside the recirculation bubble, when compared to LES results. The force increases in the outward direction, and then suddenly drops to zero in the laminar region. Notice also that there should be more turbulence activity inside the bubble for the RANS SST, as predicted by LES.

The cosine of the angle between the force results from SST and LES is plotted in the neighborhood of the plate leading edge in Fig. 14d. One can say that the force predicted by the SST model is well aligned with the LES reference data, although this does not mean that the magnitude is right. In fact most of the turbulent region present a cosine value of one (white zone). Note the black color at the shear layer and at the thin zone that separates the turbulent region from the outer laminar flow, indicating that the forces are not aligned.

Fig. 15 illustrates differences between the force results from SST and LES, where the latter is again taken as a reliable source. One can notice in Fig. 15a, the error in the shear layer region, right from its origin at the separation point. This, together with the misalignment shown in Fig. 14d, is the most important cause for the error in the prediction of the reattachment length. Inside the main bubble, there is also a prominent region in the backward flow preceding the secondary separation, where the error in the force reaches high values. To complement the information given in Fig. 15a, in Fig. 15b, the cosine of the direction of the error in the force prediction is plotted with the mean velocity from LES taken as a reference. The white and black regions in the figure correspond to locations where the over and under predicted force is accelerating and decelerating the flow respectively, or in other words, when turbulent work is being done to or by the flow. Grey areas mean the error is not changing the magnitude, but it is directly affecting the direction of velocity, either over predicting or under predicting the streamlines curvatures. It is clear from Fig. 15b that, in the initial stages of the shear layer, just after leading edge separation, the mean flow is receiving more energy from turbulence than it should. This may be the principal cause for the over prediction of the recirculation length. After this initial stage, the bubble predicted by RANS does not coincide with the bubble predicted by LES (which is the one delimited by the dash lines), and further errors do not compensate the initial over prediction.

The turbulent kinetic energy production is an important term in all RANS viscosity models that need a transport equation for the turbulent kinetic energy, k. Fig. 16 shows the error in the prediction of this term for the SST model, relative to the one calculated from
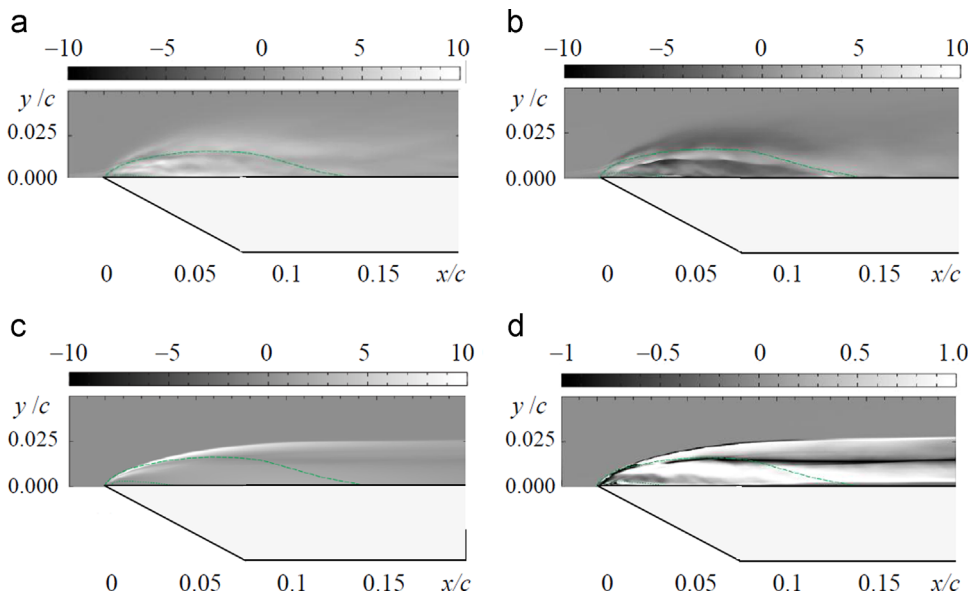

Fig. 14. Turbulent forces. (a) LES: magnitude of the turbulent force. (b) LES: component of the turbulent force aligned with the mean velocity field. (c) SST: magnitude of the turbulence force. (d) Cosine of the angle between the force results from LES and from SST.
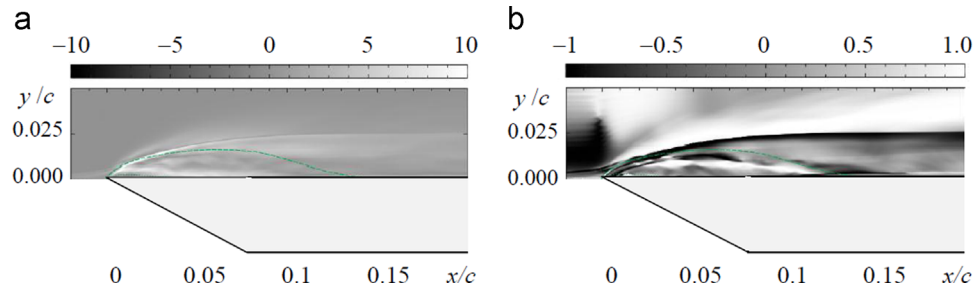
Fig. 15. Difference between LES and SST turbulence force. (a) Magnitude of the difference in turbulence force. (b) Cosine of the angle between the error in the force and the mean velocity from LES.
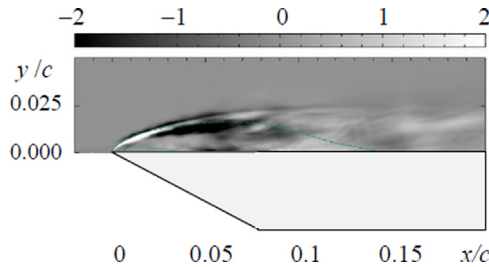

Fig. 16. Error in the turbulent energy production term.

Fig. 17. Vortices' coherent structures by criteria Q.

large eddy simulations. From this figure, it appears that, in the shear layer initial stages, production is under predicted – dash line is in the grey–black area, close to the leading edge. The isolated effect of this is that the turbulent kinetic energy will be smaller than it should, whose tendency is likely followed by the eddy viscosity. The deficit in this quantity makes the bending of the streamline less drastic, elongating the main bubble. The turbulent kinetic energy tends to be higher inside the main bubble, just below the dividing streamline, as evidenced by the white stripe. This stripe ends up crossing the dash line, but this should be attributed to the differences in the bubble frontier from LES and SST. Also of interest is the black region in the back flow preceding the expected secondary separation. This would lead to re-laminarization of the boundary layer, which should help the expected new separation. However, the SST model was not able to capture this second separation which points to other problems not contemplated here, like the inadequacy of the Boussinesq hypothesis and the lack of a more complete and objective description of the Reynolds stress tensor (Thompson, 2008).

Fig. 17 shows a side view of the plate with the coherent structures according to the Q criteria. There are two clearly distinct regions: the top turbulent zone corresponds to the outer shear layer, which is part of the main bubble; a smaller region of high turbulence levels, but not as high as this external one, which is found inside this top turbulent zone, close to the plate, and corresponds to the secondary recirculation bubble. From the direction of increasing entropy, one can see that the top region develops from left to right, while the inside structures develop from right to left, following the backward flow. Also it is interesting to note how long the shear layer took to transition to turbulence in the top turbulent zone, close to the leading edge. Certainly, for higher Reynolds numbers, the transition point would be much closer to the leading edge, but apparently this delay in transition was still small enough to make the solution accurate and Reynolds number independent. According to experimental data (Crompton, 2001) the flow becomes Reynolds number independent for $Re > 1 \times 10^5$.
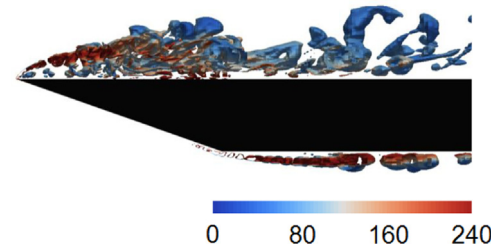
separation bubbles, but it also proved to be a challenging test case for numerical simulation of turbulence for external flows.

A thin flat plate at small incidence was used to evaluate Reynolds average Navier Stokes (RANS) models in their ability to capture highly anisotropic turbulence, like the one formed in long recirculation bubble. Large Eddy simulations were also performed and presented here, to support and complement the experimental data.

The bubble length, the pressure suction peak, the secondary recirculation, and the post-reattachment development were among the most challenging flow features for all tested RANS models.

Although the RSM presented the best prediction of the reattachment point, anomalous streamlines were obtained, as previously reported for other types of flow. Amongst the several RANS models tested, the $k-\omega$ SST has shown to be one of the best overall. For practical industrial applications, this model can be considered satisfactory. However, it still presented several imperfections that may not be tolerated in some more crucial applications.

From large Eddy simulations comparisons, it was possible to evaluate and locate the errors in modeling, either directly in terms of the expected turbulent forcing, or indirectly from the deficit in the prediction of the turbulent kinetic energy production term, that contributes to the evolution equations.

The results suggested that RANS models can be used to estimate mean quantities, but they fail to capture second order statistics. RANS models are able to capture the correct alignment of the force representing the fluctuation activities, but they fail to determine its correct magnitude, causing the mean flow to receive more energy from turbulence than it should, which leads to a poor prediction of the pressure suction in the recirculating bubble. Although the second order statistic is necessary for the correct determination of mean flow quantities, for most industrial applications, the correct behavior of the mean quantities is enough for an efficient design and the RANS model is adequate. Especially for the present type of flow the $k-\omega$ SST showed to be a good option.

6. Final remarks

The turbulent flow around thin plates is not only extremely relevant to the aerospace industry and to the understanding of airfoil

Acknowledgment

References

ANSYS CFX-Solver Theory Guide, 2013. v. 14.5, Ansys Inc.

ANSYS FLUENT, 2013. Fluent 14.5 Documentation. Fluent Inc., Software Version 14.5.0.

Cazalbou, J.B., Spalart, P.R., Bradshaw, P., 1993. On the behavior of 2-equation models at the edge of a turbulent region. Phys. Fluids 6 (5), 1797–1804.

Choi, H., Moin, P., 1994. Effects of the computational time step on numerical solutions of turbulent flow. J. Comput. Phys. 113, 1–4.

Collie, S., Gerritsen, M., Jackson, P., 2008. Performance of two-equation turbulence models for flat plate flows with leading edge bubbles. J. Fluids Eng. 130 (2), 021201-1–021201-11.

Crompton, M.J., 2001. The Thin Airfoil Leading Edge Separation Bubble (Ph.D. thesis). Department of Aerospace Engineering University of Bristol, UK.

Cyr, S., Newman, B.G., 1996. Flow past two-dimensional membrane aerofoils with rear separation. J. Wind Eng. Ind. Aerodyn. 63 (1–3), 1–16.

Germano, M., Piomelli, U., Moin, P., Cabot, W.H., 1991. A dynamic subgrid-scale eddy viscosity model. Phys. Fluids A 3 (7), 1760–1765.

Han, X., Sagaut, P., Lucor, D., 2012. On sensitivity of RANS simulations to uncertain turbulent inflow conditions. Comput. Fluids 61, 2–5.

Hanjalic, K., Jakirlic, S., 1998. Contribution towards the second-moment closure modeling of separating turbulent flows. Comput. Fluids 27 (2), 137–156.

Lasher, W.C., Sonnenmeier, J.R., Forsman, D.R., Tomcho, J., 2005. The aerodynamics of symmetric spinnakers. J. Wind Eng. Ind. Aerodyn. 93 (4), 311–337.

Lasher, W.C., Sonnenmeier, J.R., 2008. An analysis of practical RANS simulations for spinnaker aerodynamics. J. Wind Eng. Ind. Aerodyn. 96 (2), 143–165.

Laurent, C., Mary, I., Gleize, V., Lerat, A., Arnal, D., 2012. DNS database of a transitional separation bubble on a flat plate and application to RANS modeling validation. Comput. Fluids 61, 21–30.

Lian, Y.S., Shyy, W., 2005. Numerical simulations of membrane wing aerodynamics for micro air vehicle applications. J. Aircr. 42 (4), 865–873.

Lilly, D.K., 1992. A proposed modification of the Germano subgrid-scale closure method. Phys. Fluids A 4 (3), 633–635.

Menter, F.R., 1994. Two-equation eddy-viscosity turbulence models for engineering applications. AIAA J. 32 (8), 1598–1605.

Menter, F.R., Langtry, R.B., Likki, S.R., Suzen, Y.B., Huang, P.G., Volker, S., 2006. A correlation-based transition model using local variables – Part I: model formulation. J. Turbomach. ASME 128 (3), 413–422.

Newman, B.G., Tse, M.C., 1992. Incompressible-flow past a flat-plate aerofoil with leading-edge separation bubble. Aeronaut. J. 96 (952), 57–64.

Rezende, A.L.T., 2009. Numerical Investigation of the Turbulent Flow Separation Bubble over Inclined Thin Flat Plate (in Portuguese) (Ph.D. thesis). Department of Mechanical Engineering, PUC-Rio, Rio de Janeiro, RJ, Brazil.

Sampaio, L.E.B., 2006. Large Eddy Simulations of the Thin Plate Separation Bubble at Shallow Incidence (in Portuguese) (Ph.D. thesis). Department of Mechanical Engineering, PUC-Rio, Rio de Janeiro, RJ, Brazil.

Spalart, P., Allmaras, S., 1992. A one-equation turbulence model for aerodynamic flowsTechnical Report AIAA-92-0439American Institute of Aeronautics and Astronautics.

Thompson, R.L., 2008. Some perspectives on the dynamic history of a material element. Int. J. Eng. Sci. 46, 224–249.